

RESEARCH ARTICLE

Fast synthesis of NaNbO₃ nanoparticles with high photocatalytic activity for degradation of organic dyes

Daiane Fernandes¹  | Mateus M. Ferrer¹ | Cristiane W. Raubach¹ |
 Mario L. Moreira^{1,2}  | Pedro L. G. Jardim^{1,2} | Eduardo Ceretta Moreira³ |
 Carlos F. O. Graeff^{4,5} | Sergio S. Cava^{1,2} 

¹Post-Graduate Program in Materials Science and Engineering, Federal University of Pelotas, Pelotas, Rio Grande do Sul, Brazil

²Post-Graduate Program in Physics, Federal University of Pelotas, Capão do Leão, Rio Grande do Sul, Brazil

³Spectroscopy Laboratory, Federal University of Pampa, Bagé, Rio Grande do Sul, Brazil

⁴Post-Graduate Program in Materials Science and Technology, São Paulo State University, Bauru, São Paulo, Brazil

⁵Department of Physics, São Paulo State University, Bauru, São Paulo, Brazil

Correspondence

Daiane Fernandes, Post-Graduate Program in Materials Science and Engineering, Federal University of Pelotas, 96010–610, Pelotas, RS, Brazil.
 Email: daiane.fg.eng@outlook.com

Funding information

Coordenação de Aperfeiçoamento de Pessoal de Nível Superior; Conselho Nacional de Desenvolvimento Científico e Tecnológico; Fundação de Amparo à Pesquisa do Estado do Rio Grande do Sul, Grant/Award Number: 17/25510000889-8

Abstract

NaNbO₃ nanoparticles were obtained using the microwave-assisted hydrothermal method followed by heat treatment. It has been shown that heat treatment to increase the crystallinity of the material and modifies particle shape, from nanowires to nanograins. Nanowires with a diameter of approximately 35 nm and a length of tens of micrometers were obtained in the shortest time ever reported in the literature. Particles in the shape of nanograins with a diameter of approximately 35 nm were obtained by burning the nanowires. The photocatalytic activity of the nanoparticles was investigated through the photodegradation of Rhodamine B dye. Electronic structure analysis using density functional theory (DFT) along with experimental techniques was performed to help understand the photocatalytic activity of each sample. The obtained nanoparticles were highly favorable for photocatalytic applications, especially the nanograins, which degraded 100% of the dye in 50 min.

KEYWORDS

dye degradation, nanoparticles, photocatalysis, sodium niobate

1 | INTRODUCTION

Currently, the planet is undergoing progressive technological development and population density, resulting in increased generation of various effluents. Therefore, it is necessary that they receive the appropriate treatment to be degraded into harmless substances or less toxic to the environment and to humans. Among the different treatment methods, the advanced oxidative processes have received

increasing attention, because they can totally or partially degrade compounds that are difficult to degrade,¹ mainly originating from the textile and pharmaceutical industry.

Heterogeneous photocatalysis is one of the most applied oxidative methods and had its mechanism explained in 1972, by Japanese researchers Fujishima and Honda, who reported the division of water molecules using as photocatalyst the semiconductor titanium dioxide.² In this type of process, the semiconductor when absorbing photons

with energy equal to or greater than its band gap value has its electrons excited from the valence band (VB) to the conduction band (CB), generating an electron/hole pair, thus forming oxidizing and reducing sites on its surface, degrading in turn several pollutants.

Although heterogeneous photocatalysis is a promising and sustainable approach to environmental remediation, existing photocatalysts still face major limitations, for example, the fast recombination of photoinduced charge carriers, limiting photocatalytic activity. For this purpose, great advances have been made using the strategy of building heterostructures, which allows the migration of charges between the materials involved, causing this spatial separation to prevent their rapid recombination.^{3–11} Other factors also contribute to the performance of photocatalysts such as crystal structure, particle shape, electronic structure, and others.¹² It is also known that the reduction of the diffusion length is interesting, because the smaller the particle, the smaller the transfer distance of the photogenerated electron to the surface, also because the particle ends up having a high surface/volume ratio and a kinetically desirable structure.¹³ This makes nanoscale particles very promising for this application.

Sodium niobate (NaNbO_3) is a semiconductor that has Perovskite crystal structure, that is, has ABX_3 type stoichiometry, where the A and B sites are occupied by metallic cations, and the X site is occupied by an element of the nonmetals group.¹⁴ It has many technological application properties, and, among them, the photocatalytic applications presented in the literature showed excellent results.^{13,15–23} Being a promising photocatalyst because it is thermodynamically stable, has high corrosion resistance, and is nontoxic.^{22,24} However, studies have shown that the natural particle shape of NaNbO_3 is cubic and presents low photocatalytic activity, but in syntheses with hydrothermal conditions followed by heat treatment, it is possible to obtain the semiconductor in the form of nanowires, with high photocatalytic activity.^{15,18,21,25}

Under hydrothermal conditions, before the formation of NaNbO_3 , a metastable phase of sodium hexaniobate nanowires is formed ($\text{Na}_2\text{Nb}_2\text{O}_6 \cdot \text{H}_2\text{O}$), and as the synthesis process progresses, the process of nucleation of the crystals in the form of cubes on the wires occurs, through the Ostwald ripening.^{18,25–29} To obtain Perovskite in the shape of nanowires, it is necessary that its nucleation takes place in a confined space, with short-range diffusion, as is the heat treatment step.¹⁸ Therefore, to obtain NaNbO_3 in the form of nanowires, it is necessary to synthesize $\text{Na}_2\text{Nb}_2\text{O}_6 \cdot \text{H}_2\text{O}$ and apply a subsequent heat treatment.^{18,25–29}

To date, NaNbO_3 particles in the form of nanowires are extensively studied, as they are considered the most

promising for photocatalytic applications. Several research has been devoted to elucidating its growth process and comparing it with the natural cubic particle. However, Farooq et al.¹³ obtained nanoparticles with a grain/cuboid shape with sizes between 5 and 30 nm, with high photocatalytic activity. The nanoparticles were obtained by the polymeric citrate precursor method, for 22 h and then calcined for 12 h. Given the above, it is highly desirable to study other synthesis routes, preferably faster, to obtain this type of nanoparticle and compare with the nanowires. Therefore, in the present work, we present a shorter time route to obtain NaNbO_3 nanowires, and we demonstrated that it is possible to obtain nanoparticles similar to those reported by Farooq et al.,¹³ in a shorter time as well, through the “breaking” of these nanowires. The samples obtained had their photocatalytic activity measured through the photodegradation of Rhodamine B (RhB), a dye widely used in industries and known for its high toxicity, good stability, and nonbiodegradability.³⁰ An analysis of electronic structure using first-principles calculations based on density functional theory (DFT) together with experimental techniques were performed to understand the photocatalytic activity of each sample. Therefore, in the present work, we present a shorter time route to obtain NaNbO_3 nanowires, through microwave-assisted hydrothermal synthesis, followed by a heat treatment process. The heat treatment was carried out at temperatures between 300 and 800°C, to analyze the influence on the crystalline structure, electronic structure, particle shape, and photocatalytic activity, which was measured through the photodegradation of Rhodamine B (RhB), a dye widely used in industries and known for its high toxicity, good stability, and nonbiodegradability.³⁰ An analysis of electronic structure using first-principles calculations based on DFT together with experimental techniques was performed to understand the photocatalytic activity of each sample.

2 | EXPERIMENTAL PROCEDURE

2.1 | Sample preparation

The samples were obtained according to the synthesis presented in a previous study,³¹ with some modifications. NaOH (Merck, 99.0%) and NbCl_5 (Brazilian Mining and Metallurgy Company, 99.0%) were solubilized in distilled water by magnetic stirring at room temperature, with concentrations of 6 M and 0.6 M, respectively. This solution was heated at 180°C in the adapted microwave (800 W, 2.45 GHz, PANASONIC) for 15 min. The precipitate obtained was washed and centrifuged until the pH was neutralized and then oven dried overnight.

The final powder was submitted to a thermal treatment in a tubular oven at 300–800°C during 2 h using a heating rate of 10°C/min and naturally cooled to room temperature.

2.2 | Sample characterization

The thermal analyzes were investigated using a (thermogravimetry-differential thermal- derived thermogravimetry) TG-DTA-DTG equipment (STA449F3, NETZSCH), with atmosphere controlled by nitrogen. X-ray diffraction (XRD) was performed using a diffractometer (Ultima IV, RIGAKU) with Cu-K α radiation ($\lambda = 1.5406 \text{ \AA}$), scanning from 2θ of 10–90° with speed of 10°/min. Micrographs were obtained by scanning electron microscopy (SEM) using an Field Emission Gun (FEG) electron microscope (JSM7500F, JEOL). The transmission electron microscopy (TEM) images were performed in an electron microscope (CM200, PHILIPS) operated at 200 Kv. The optical gap of the samples was estimated by diffuse reflection spectroscopy by a ultraviolet-visible (UV-Vis) spectrometer (HR2000+, OCEAN OPTICS). The photoluminescence (PL) of the samples was analyzed using a fluorescence spectrometer (Cary Eclipse, AGILENT), with excitation laser of 280 nm. The surface area was estimated using equipment (Quantchrome Instrument, Nova 4200) in the presence of liquid nitrogen (77 K). The surface area was determined using the Multipoint Brunauer, Emmett and Teller equation, done automatically by the instrument.

2.3 | Photocatalytic analysis

The photocatalytic activity of each sample was evaluated through the degradation of the organic dye RhB (C₂₈H₃₁CIN₂O₃), in solution. The experiment was carried out in a closed box at a temperature of 25°C, internally lit by five ultraviolet-C lamps of 15 W each (TUV, PHILIPS, maximum intensity at 254 nm). The photocatalytic reaction was carried out with 25 mg of powder dispersed in 50 ml of RhB solution (1 \times 10⁻⁵ mol.L⁻¹), under magnetic stirring. Each sample was first stirred in the solution in the dark for 30 min, to achieve the balance between adsorption and desorption. After the light was on, aliquots of the solution were collected and centrifuged for further analysis of absorption. The variation in RhB concentration was recorded by monitoring the absorbance at 554 nm, using a UV-Vis spectrophotometer (SP200 UV, BEL PHOTONICS).

For reuse tests, each powder was separated by centrifugation after analysis, washed once with distilled water

and once with ethanol, and dried. The powders were then weighed, and the ratio between catalyst (0.5 mg) and the RhB solution (1 ml) was maintained.

2.4 | Theoretical calculations

DFT was used to evaluate the electronic structure. The simulations were performed using the CRYSTAL17 package³² with the HSE06 hybrid functional. Such a functional was selected because it generated values close to the experimental results.³³ All atomic basis was defined using Triple-Zeta Valence with Polarization Gaussian basis sets (POB-TZVP), Na center developed by Oliveira et al.³⁴ and Nb and O centers by Laun et al.³⁵ The Coulomb and exchange series thresholds (overlap and penetration for Coulomb integrals, the overlap for Hartree Fock (HF) exchange integrals, and the pseudo-overlap) used in the CRYSTAL17 package were set as 8, 8, 8, 8, 16 (10–8, 10–8, 10–8, 10–8, and 10–16). The Pack–Monkhorst and Gilat net parameters were set as 6 and 6, respectively.

The phase evaluation was performed according Rietveld refinement analysis of the XRD patterns using General Structure Analysis System (GSAS) program.³⁶ In this simulation, the background and the peak profiles were adjusted using a Chebyshev polynomial of the first kind and Thompson-Cox-Hastings pseudo-Voigt (pV-TCH), respectively.³⁷

3 | RESULTS AND DISCUSSION

3.1 | Structural and morphological characterization

Figure 1 shows the XRD patterns of the sample as prepared and with different heat treatment temperatures. The peaks observed in the sample as prepared suggest the structure reported as Na₂Nb₂O₆·H₂O, monoclinic phase, space group C2/c, with the cell parameters: $a = 17.114 \text{ \AA}$, $b = 5.0527 \text{ \AA}$, $c = 16.5587 \text{ \AA}$, and $\beta = 113.947^\circ$.^{18,25–29,31,38–46} As the heat treatment temperature of 300°C is applied, it is possible to observe that the peaks located in $2\theta = 11–14^\circ$ and $28–31^\circ$, characteristic of the Na₂Nb₂O₆·H₂O phase, begin to decrease. Raising the temperature to 400°C, and there is the appearance of the peaks of the NaNbO₃ phase. In samples treated between 500 and 800°C, only the peaks belonging to a single-phase NaNbO₃ phase are observed, orthorhombic phase, space group P21ma (JCPDS 82–606).^{13,39,47} In the sample treated 600°C is possible to observe a shift in the main peaks, possibly caused by the diffusion of sodium ions in the lattice. When this occurs, the material reduces its surface area to reduce

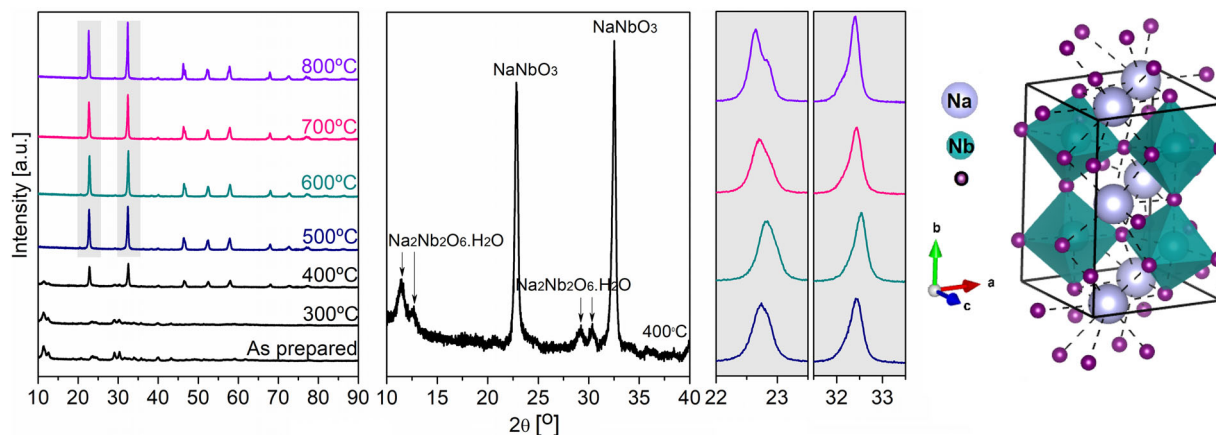


FIGURE 1 XRD patterns

free energy caused by the tension in the lattice. At 700°C, the volatilization of sodium ions occurs, and the free energy decreases, and the surface area increases again. This behavior is seen in the samples, as presented in Section 3.5. In addition, the mean value of the crystallographic domains was estimated by the Scherrer equation, resulting in 21.90, 23.13, 24.05, and 27.43 nm for the NaNbO_3 samples treated at 500, 600, 700, and 800°C, respectively. This demonstrates an increase in crystallinity as the temperature rises, as can be seen by the more defined diffraction peaks as well. The crystalline phase of the NaNbO_3 samples was confirmed by Rietveld refinement (Figure S1, Table S1). All samples showed good convergence to the orthorhombic phase P21ma, according to χ^2 and RBragg (Table S2).

To better understand the processes involved in the formation and transformation of the Perovskite phase, a TG-DTA-DTG thermal analysis was performed, shown in Figure 2. Through the TG curve, an initial mass loss is observed that occurs until the temperature of 181°C, this activity corresponds to the evaporation of the water adsorbed on the surface of the $\text{Na}_2\text{Nb}_2\text{O}_6 \cdot \text{H}_2\text{O}$. Between the temperatures of 181 and 305°C, an endothermic peak is observed, accompanied by another loss of mass, this activity corresponds to the dehydration of the $\text{Na}_2\text{Nb}_2\text{O}_6 \cdot \text{H}_2\text{O}$.^{18,25–29,31,38–46} The DTA curve shows a sharp exothermic peak in the temperature range between 487 and 549°C, without mass loss indicating the complete formation of the NaNbO_3 phase, result compatible with that observed in XRD (Figure 1). From 620°C, an endothermic event is observed in the DTA curve with a mass loss, indicating that from this temperature onward, the volatilization of sodium ions occurs. At high temperatures, the evaporation of alkaline ions is high.^{47,48}

Micrographs of the sample as prepared and at different heat treatment temperatures are shown in Figure 3. The sample as prepared (Figure 3A) has a nanowire particle

shape, compatible with $\text{Na}_2\text{Nb}_2\text{O}_6 \cdot \text{H}_2\text{O}$ ^{18,25–29,38–46}, with an average diameter of approximately 35 nm and a length of tens of micrometers. With heat treatment at 500°C (Figure 3B), where the complete formation of NaNbO_3 occurs, the shape of nanowires is preserved, without significant changes. When the temperature is raised to 600°C (Figure 3C) and 700°C (Figure 3D), it is possible to observe that the nanowires begin to break and turn into smaller particles, due to the rearrangement of crystals.^{47,49} In the sample treated at 800°C (Figure 3E), particles in the form of nanowires are no longer observed, but a nanograin-like particle with an average diameter of approximately 35 nm. In addition, TEM was performed on the samples treated at 500°C (Figure 3F) and 800°C (Figure 3G), to better observe the morphological aspects and the size of the nanoparticles. Through this analysis, it is observed that both sample present shape and size consistent with the micrographs obtained by SEM.

Gu et al.⁴⁷ presented a study, where through a solvothermal synthesis, at 230°C for 16 h, using isopropanol as a reaction medium, obtained 1D particles of $\text{Na}_7(\text{H}_3\text{O})\text{Nb}_6\text{O}_{19} \cdot 14\text{H}_2\text{O}$. That after being subjected to heat treatment for 4 h, at different temperatures with a maximum of 800°C, gave rise to NaNbO_3 particles with the same particle shape transformation process obtained in this work. However, the precursor $\text{Na}_7(\text{H}_3\text{O})\text{Nb}_6\text{O}_{19} \cdot 14\text{H}_2\text{O}$ presented a larger particle diameter, approximately 193.2 nm, resulting in NaNbO_3 1D with a diameter of approximately 305.1 nm and NaNbO_3 in the form of ellipsoids with a width and length of approximately 512.3 and 548.6 nm, respectively. Therefore, we can observe with this study that the 1D precursor of $\text{Na}_2\text{Nb}_2\text{O}_6 \cdot \text{H}_2\text{O}$ originates 1D NaNbO_3 particles with very small diameter, and by raising the heat treatment temperature above 700°C, it was possible to obtain even smaller particles, highly desirable for photocatalytic applications. Furthermore, given the results presented, it is

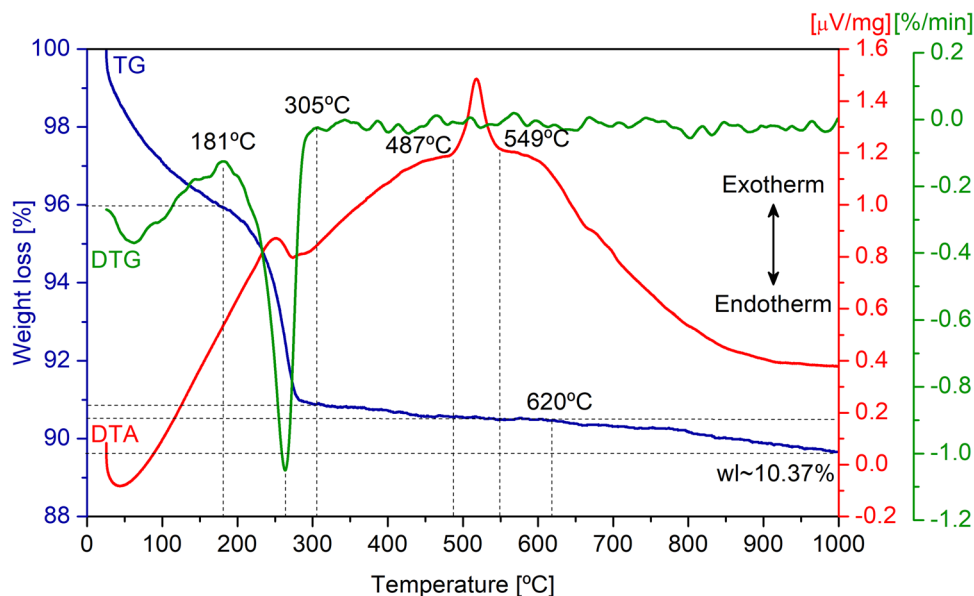


FIGURE 2 TG-DTA-DTG curves

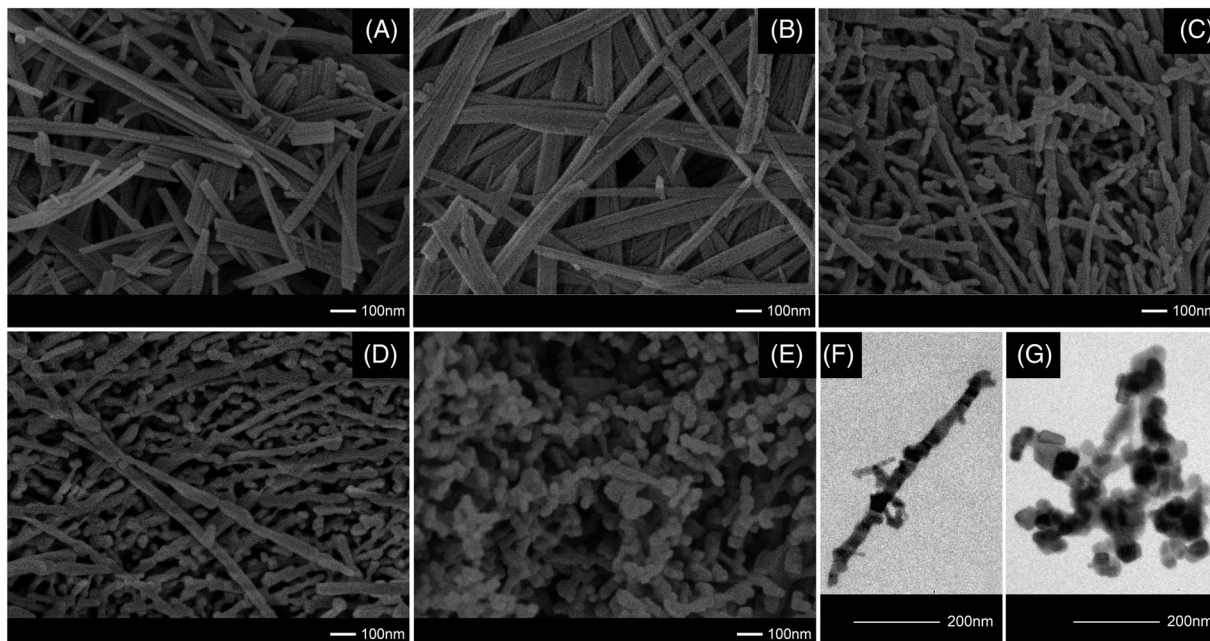


FIGURE 3 SEM: (A) as prepared, (B) 500°C, (C) 600°C, (D) 700°C, (E) 800°C, and TEM: (F) 500°C, (G) 800°C

also possible to verify the obtaining of NaNbO_3 nanowires in a shorter time already reported in the literature (Table 1).

3.2 | Photocatalytic performance

3.2.1 | Photocatalytic activity

The photocatalytic activity of each NaNbO_3 sample was evaluated by the degradation of the RhB dye in solution,

as described in the experimental procedure. Figure 4A shows the dye concentration curves over the analysis time, where C_0 and C indicate the initial concentration of RhB and concentration at a specific time (min), respectively. Through the dye curve, without the semiconductor, it is observed that has a very low photolysis process. Photocatalytic activity is increased using the samples treated with higher heat treatment temperature, reaching maximum dye removal in 50 min. All samples showed high photocatalytic activity, reaching a maximum percentage of dye degradation of 100% and minimum of 72% in a period of

TABLE 1 Synthesis that obtained NaNbO_3 nanowires

Synthesis method, temperature/time	Heat treatment, temperature/time	Reference
HID-C 183°C/2 h	600°C/6 h	Alexandre et al. [32]
HID-AM 150°C/1 h	350°C/2 h	Fernandes et al. [22]
HID-C 150°C/4 h	400°C/12 h	Jung et al. [28]
HID-C 120°C/3 h	400°C/NE	Ke et al. [18]
HID-C 180°C/2 h	300°C/12 h	Liu et al. [9]
HID-C 140°C/6 h	700°C/3 h	Pei et al. [35]
HID-C 200°C/24 h	550°C/4 h	Shi et al. [12,16]
HID-AM 180°C/60 min	550°C/4 h	Teixeira et al. [20]
HID-AM 180°C/30 min	550°C/4 h	Teixeira et al. [31]
HID-C 200°C/8 h	400°C/3 h	Wang et al. [33]
HID-C 160°C/6 h	NE/NE	Wang et al. [34]
HID-C 150°C/10 h	NE/NE	Yu et al. [19]
HID-C 160°C/6 h	500°C/2 h	Zhang et al. [30]

Note: HID-C (conventional hydrothermal); HID-AM (microwave-assisted hydrothermal); NE (not specified).

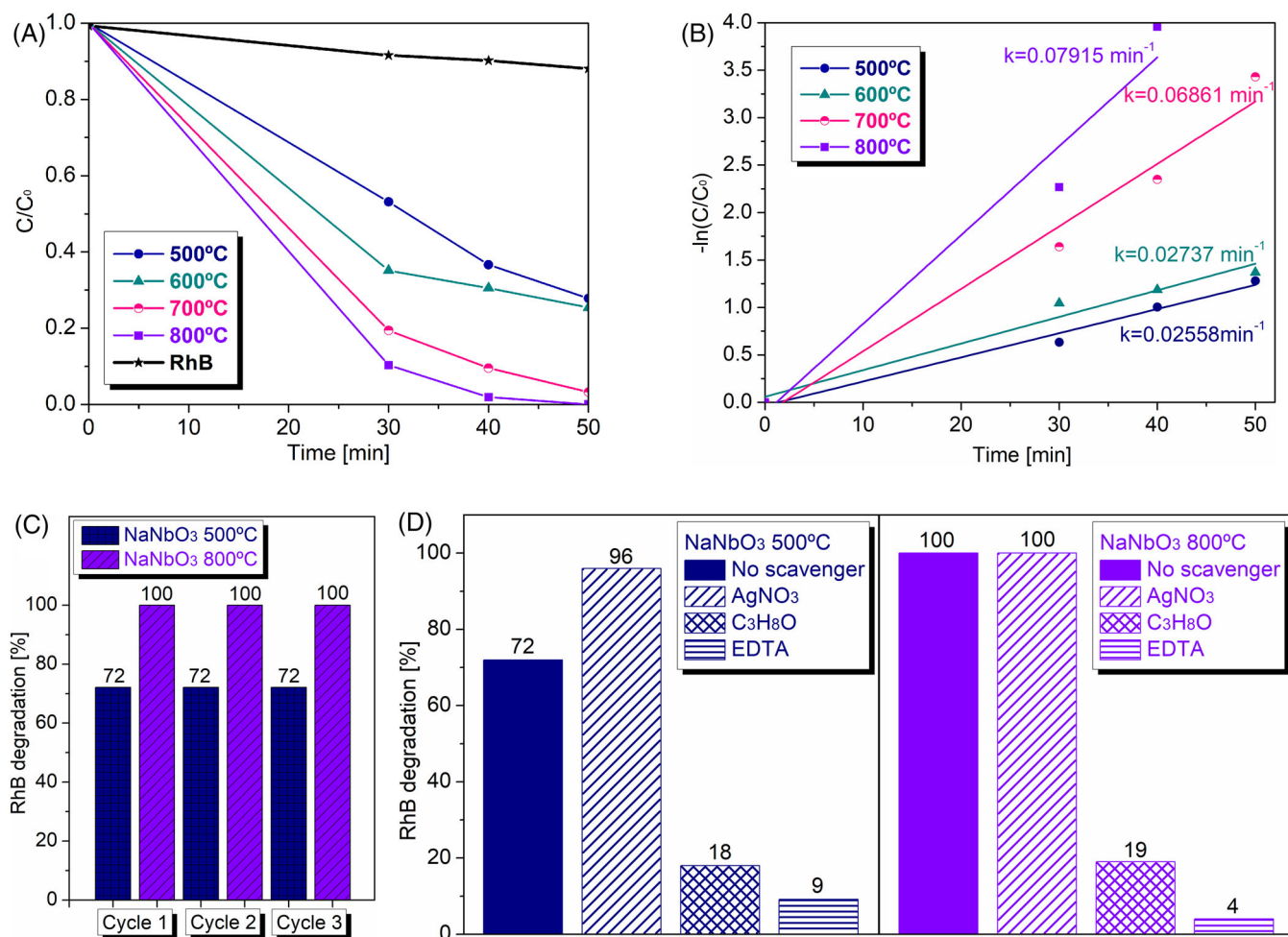


FIGURE 4 (A) Variation in the RhB concentration with time. (B) Kinetic linear simulation curves of RhB degradation. (C) Reuse of the photocatalysts for three cycles. (D) Percentage of RhB degradation using scavengers

50 min, using the sample treated at 800 and 500°C, respectively. Figure 4B shows the kinetics of RhB degradation in the presence of each sample of NaNbO₃. The reaction rate constant (*k*) was determined using the linear relationship, $-\ln(C/C_0) = kt$, where *t* is the time in minutes.¹ The results indicate that the dye degradation follows the pseudo-first order kinetics and that the sample treated at 800°C has a dye removal rate of 3.09, 2.89 and 1.5 times greater than the sample treated at 500°C, 600°C and 700°C, respectively.

3.2.2 | Photocatalytic stability

For the practical application of catalysts, the stability is of great importance. For such, a reuse experiment was carried out, using the samples treated at 500 and 800°C. After three consecutive cycles, it was possible to verify that both samples maintained the same photocatalytic performance (Figure 4C). This demonstrates that NaNbO₃ can be considered a stable and highly efficient photocatalyst.

3.2.3 | Photocatalytic mechanism

To better understand the mechanism of dye degradation in the photocatalytic process, experiments to identify the active species were performed with samples treated at 500 and 800°C. Isopropyl alcohol (C₃H₈O), silver nitrate (AgNO₃), and disodium ethylenediaminetetraacetate (EDTA) were used as scavengers for hydroxyl radicals ($\cdot\text{OH}$), electrons (e^-), and holes (h^+), respectively. Figure 4D shows the percentage of RhB degradation with the presence of scavengers at the end of 50 min. It is observed that both photocatalysts present similar behavior. The addition of EDTA and C₃H₈O inhibited the degradation of the dye, indicating that the main active species during the photocatalysis process are h^+ and $\cdot\text{OH}$. In contrast, the addition of AgNO₃ in the photocatalytic solution using the sample treated at 500°C caused an increase in the discoloration percentage of RhB, from 72% to 100%. This indicates that the restriction of e^- left a greater number of h^+ available to act in the oxidation of the dye. For the reaction using the sample treated at 800°C the percentage of discoloration was the same 100% with the addition of AgNO₃, indicating that the e^- are not active species in the photocatalysis process studied here.

3.3 | DFT calculations

Figure 5A shows the band structure orthorhombic P21ma (O-NaNbO₃). The bands demonstrate that the semiconductor O-NaNbO₃ presents a direct band gap,

with transition at point $\Gamma \rightarrow \Gamma$ and energy of the 3.6 eV. Figure 5B shows pDOS. It is observed that VB is composed mainly by the O 2p orbital and the CB by the Nb 4d orbital. Therefore, its optical gap is mainly determined by these orbitals. In both bands there is a small hybridization between the O 2p/Nb 4d, and there are almost no electronic states of Na. This electronic nature is consistent with the literature.^{20–22,50–52} The absence of electronic states of Na is due to their high ionicity, which makes it difficult to bond with other atoms by hybridization.⁵⁰

3.4 | Optical characterization

Based on information obtained from the theoretical study of electronic structure, the band gap of the samples was estimated through diffuse reflectance by the Wood/Tauc method.⁵³ Using the equation $(\alpha h\nu)^n = A(h\nu - E_g)$ where α , *h*, ν , *n*, *A*, and *E_g* are the absorption coefficient near the absorption edge, Planck's constant, frequency of light, constant related to the type of electronic transition of the material (*n* = 2 for the direct gap), proportionality constant, and band gap energy, respectively. Estimated values are shown in Figure 6A. The samples treated at 500, 700, and 800°C showed a band gap of 3.50, 3.52 eV, and 3.55 eV, respectively. This increase occurs due to the increase in crystallinity, as shown by the calculation of crystallographic domains, as the bands are better delimited, making the superposition of wave functions more defined. However, the sample treated at 600°C has a band gap of 3.45 eV. This band gap reduction in the material is a consequence of the reduction of the lattice distance that generates a greater expansion of the energy level.⁵⁴ Therefore, the sample treated at 600°C has a slightly smaller band gap because it has smaller cell parameters, as shown by the deviations of diffraction peaks for larger angles, shown in Figure 1. The reduction in bandgap favors photocatalysis, as the semiconductor requires less energy to activate. However, this behavior was not observed in the samples. The band gap does not seem to significantly influence the performance of the photocatalysts studied here.

To complement the understanding of the photocatalytic activity variation between the samples, PL spectroscopy technique was performed, that allows to know the behavior of the recombination of the electron-hole pairs, important criterion for understanding the performance of photocatalysts. The PL emission spectra are shown in Figure 6B. All samples showed similar behavior, with broadband PL in the region between 300 and 450 cm⁻¹, with main emission peaks at 362 and 383 nm, corresponding to an energy of 3.42 and 3.24 eV, respectively. This broadband emission indicates that the recombination takes place by a multiphonon process, in other words, the

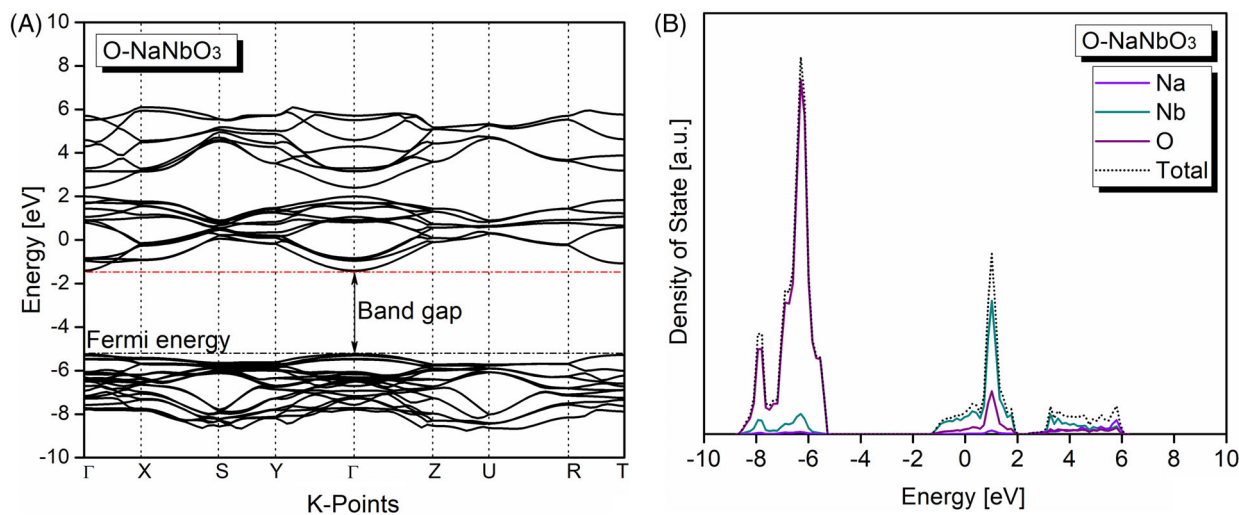


FIGURE 5 (A) Calculated band structure of NaNbO_3 , (B) The pDOS of the NaNbO_3

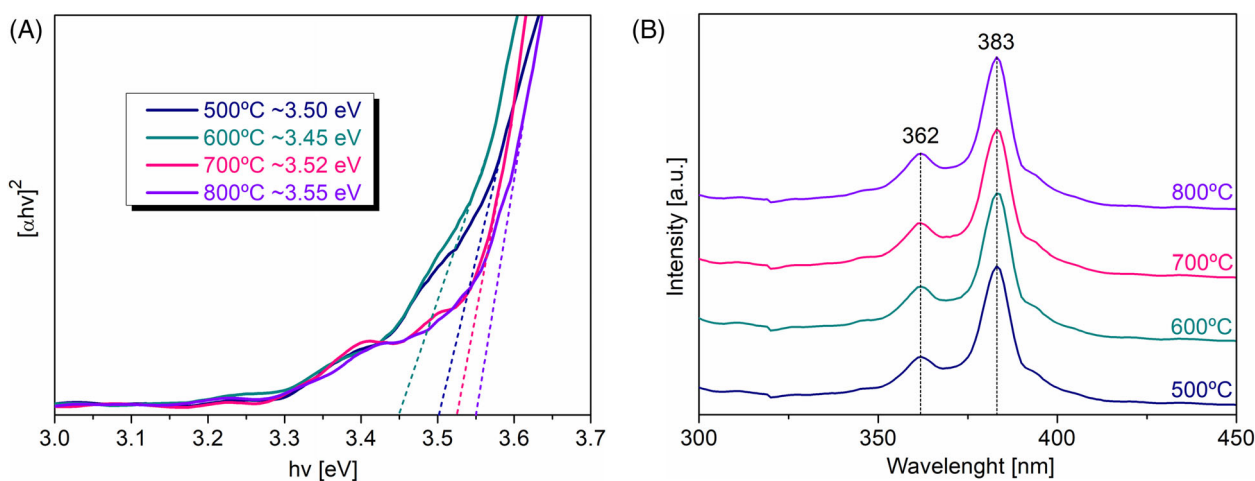


FIGURE 6 A. Band gap of the NaNbO_3 samples. (B) Photoluminescence curves of the NaNbO_3 samples

relaxation occurs with the participation of various energy states, caused by intrinsic defects in the material.^{55,56} These intermediate electronic levels are associated with shallow defects, of surface, responsible for the emission of PL in regions of high energy (violet/blue).⁵⁷ The presence of these defects favors photocatalysis, because they delay recombination of the photogenerated electron/hole pair. This indicates that the increase in photocatalytic activity is related to the crystallinity of the samples. The more crystalline the lattice, the lower the rate of recombination of the photogenerated charges.

3.5 | Surface area analysis

Another important factor that affects photocatalytic activity is surface area. It is known that the greater the surface

area of the catalyst, the greater the probability of available and accessible active sites and also dye adsorption sites.^{13,58} As shown in Section 3.1, the sample treated at 600°C showed a deviation in the diffraction peaks, possibly caused by the diffusion of sodium ions in the lattice. When this occurs, the material reduces its surface area to reduce free energy caused by the tension in the lattice. When the temperature is raised, the volatilization of the alkali metal decreases the free energy, and the area increases again. This behavior is seen in the samples, which presented surface areas of 28 m²/g, 11 m²/g, 31 m²/g, and 32 m²/g for temperatures of 500, 600, 700, and 800°C, respectively. The increase in surface area is also a consequence of the change in particle shape. Sodium volatilization detaches the crystals initially arranged in the nanowires that “break” turning into smaller particles with the shape of nanograins (Figure 3).

Although the sample treated at 500°C had a surface area more than twice that of the sample treated at 600°C, its photocatalytic activity was lower. This demonstrates that even the surface area being a determining factor for most photocatalysts, it does not directly influence these NaNbO_3 samples. The nanograins obtained at 800°C showed a slightly larger area compared to the nanowires at 500°C, and we observed that their photocatalytic performance was superior. This possibly occurs because the decrease in particle size leads to a reduction in the recombination of charge carriers, as the migration time to the surface is proportional to the square of the particle size.⁵⁹ Small particles also have more atoms with incomplete coordination, which makes them more reactive. This demonstrates that particle shape appears to play a very important in photocatalytic activity.


4 | CONCLUSIONS

In this study, we propose a method to obtain NaNbO_3 nanowires through the microwave-assisted hydrothermal system, followed by heat treatment, in a shorter time. We demonstrated that with a simple heat treatment it was possible to change the shape of the particles, from nanowires to nanograins. The heat treatment increased the crystallinity of the samples without modifying the phase. All samples showed high photocatalytic activity, especially the nanograins. It was found that the factors that influence the performance of the samples studied here were the crystallinity and shape of the particle. Reuse tests demonstrated the stability of the photocatalysts. Therefore, this study contributes information to obtain highly favorable nanoparticles NaNbO_3 for photocatalytic applications.

ACKNOWLEDGMENTS

The authors thank Companhia Brasileira de Metalurgia e Mineração (CBMM) for donating the niobium precursor, Núcleo de Apoio à Pesquisa em Ciência e Engenharia de Materiais (NAPCEM-UNIFESP Campus São José dos Campos) for XRD and BET analysis, Laboratory of Thermal Analysis - Department of Chemistry (UNESP Campus Bauru) for TG-DTG-DTA analysis, and colleagues Thissiana Fernandes, Paola Gay, Ramon Dadalto, Silvia Cucatti, Luciano Gularte, Catia Ucker, Caroline Schmechel, Lucas Barcellos, Cristian Fernandes, and Fabio Riemke for their support in laboratory activities. This research received support from Coordenação de Aperfeiçoamento de Pessoal de Nível Superior (CAPES), Conselho Nacional de Desenvolvimento Científico e Tecnológico (CNPq), and Fundação de Amparo à Pesquisa do Estado do Rio Grande do Sul (FAPERGS) (17/25510000889-8).

ORCID

Daiane Fernandes  <https://orcid.org/0000-0002-1604-2198>

Mario L. Moreira  <https://orcid.org/0000-0002-0588-3717>

Sergio S. Cava  <https://orcid.org/0000-0002-0907-7739>

REFERENCES

1. Ücker CL, Goetzke V, Almeida SR, Moreira EC, Ferrer MM, Jardim PLG, et al. Photocatalytic degradation of rhodamine B using Nb_2O_5 synthesized with different niobium precursors: factorial design of experiments. *Ceram Int.* 2021;47(14):20570–8.
2. Fujishima A, Honda K. Electrochemical photolysis of water at a semiconductor electrode. *Nature.* 1972;238:37–8.
3. Li S, Hu S, Jiang W, Zhang J, Xu K, Wang Z. In situ construction of WO_3 nanoparticles decorated Bi_2MoO_6 microspheres for boosting photocatalytic degradation of refractory pollutants. *J Colloid Interface Sci.* 2019;556:335–44.
4. Li S, Chen J, Hu S, Wang H, Jiang W, Chen X. Facile construction of novel $\text{Bi}_2\text{WO}_6/\text{Ta}_3\text{N}_5$ Z-scheme heterojunction nanofibers for efficient degradation of harmful pharmaceutical pollutants. *Chem Eng J.* 2020;402:126165.
5. Li S, Wang C, Liu Y, Xue B, Jiang W, Liu Y, et al. Photocatalytic degradation of antibiotics using a novel $\text{Ag}/\text{Ag}_2\text{S}/\text{Bi}_2\text{MoO}_6$ plasmonic p-n heterojunction photocatalyst: mineralization activity, degradation pathways and boosted charge separation mechanism. *Chem Eng J.* 2021;415:128991.
6. Li S, Wang C, Liu Y, Cai M, Wang Y, Zhang H, et al. Photocatalytic degradation of tetracycline antibiotic by a novel $\text{Bi}_2\text{Sn}_2\text{O}_7/\text{Bi}_2\text{MoO}_6$ S-scheme heterojunction: performance, mechanism insight and toxicity assessment. *Chem Eng J.* 2022;429:132519.
7. Wang C, Cai M, Liu Y, Yang F, Zhang H, Liu J, et al. Facile construction of novel organic–inorganic tetra (4-carboxyphenyl) porphyrin/ Bi_2MoO_6 heterojunction for tetracycline degradation: performance, degradation pathways, intermediate toxicity analysis and mechanism insight. *J Colloid Interface Sci.* 2022;605:727–40.
8. Wang C, Li S, Cai M, Yan R, Dong K, Zhang J, et al. Rationally designed tetra (4-carboxyphenyl) porphyrin/graphene quantum dots/bismuth molybdate Z-scheme heterojunction for tetracycline degradation and Cr(VI) reduction: performance, mechanism, intermediate toxicity appraisalment. *J Colloid Interface Sci.* 2022;619:307–21.
9. Li S, Wang C, Cai M, Yang F, Liu Y, Chen J, et al. Facile fabrication of $\text{TaON}/\text{Bi}_2\text{MoO}_6$ core-shell S-scheme heterojunction nanofibers for boosting visible-light catalytic levofloxacin degradation and Cr(VI) reduction. *Chem Eng J.* 2022;428:131158.
10. Li S, Cai M, Wang C, Liu Y, Li N, Zhang P, et al. Rationally designed $\text{Ta}_3\text{N}_5/\text{BiOCl}$ S-scheme heterojunction with oxygen vacancies for elimination of tetracycline antibiotic and Cr(VI) : performance, toxicity evaluation and mechanism insight. *J Mater Sci Technol.* 2022;123:177–90.
11. Li S, Cai M, Liu Y, Zhang J, Wang C, Zang S, et al. In situ construction of a C_3N_5 nanosheet/ Bi_2WO_6 nanodot S-scheme heterojunction with enhanced structural defects for the efficient photocatalytic removal of tetracycline and Cr(vi) . *Inorg Chem Front.* 2022;9:2479–97.

12. Grabowska E. Selected perovskite oxides: characterization, preparation and photocatalytic properties-a review. *Appl Catal B: Environ.* 2016;186:97–126.
13. Farooq U, Phul R, Alshehri S, Ahmed J, Ahmad T. Electro-catalytic and enhanced photocatalytic applications of sodium niobate nanoparticles developed by citrate precursor route. *Sci Rep.* 2019;9:4488.
14. Giorgi G, Yamashita, K Organic-inorganic halide perovskites: an ambipolar class of materials with enhanced photovoltaic performances. *J Mater Chem A.* 2015;3(17):8981–91.
15. Yan C, Li B, Wang J. A comparative study of photodegradation behavior sodium niobate nanowires and microcubes. *Key Eng Mater.* 2020;861:221–7.
16. Van ND. Template-free synthesis and photocatalytic activity of {001}-facets exposed rhombohedral NaNbO₃ microcrystals. *Ceram Int.* 2018;44(16):19945–9.
17. Li G, Yi Z, Bai Y, Zhang W, Zhang H. Anisotropy in photocatalytic oxidation activity of NaNbO₃ photocatalyst. *Dalton Trans.* 2012;41(34):10194–8.
18. Liu Q, Zhang L, Chai Y, Dai WL. Facile fabrication and mechanism of single-crystal sodium niobate photocatalyst: insight into the structure features influence on photocatalytic performance for H₂ evolution. *J Phys Chem C.* 2017;121(46):25898–907.
19. Nawaz M, Almofty SA, Qureshi F. Preparation, formation mechanism, photocatalytic, cytotoxicity and antioxidant activity of sodium niobate nanocubes. *PLoS One.* 2018;13(9):e0204061.
20. Hamilton A, O'donnell S, Zoellner B, Sullivan I, Maggard PA. Flux-mediated synthesis and photocatalytic activity of NaNbO₃ particles. *J Am Ceram Soc.* 2019;103(1):454–64.
21. Shi H, Wang T, Chen J, Zhu C, Ye J, Zou Z. Photoreduction of carbon dioxide over NaNbO₃ nanostructured photocatalysts. *Catal Lett.* 2011;141:525–30.
22. Li P, Ouyang S, Xi G, Kako T, Ye J. The effects of crystal structure and electronic structure on photocatalytic H₂ evolution and CO₂ reduction over two phases of perovskite-structured NaNbO₃. *J Phys Chem C.* 2012;116(14):7621–8.
23. Fresno F, Jana P, Reñones P, Coronado JM, Serrano DP, de la Peña O'Shea VA. CO₂ reduction over NaNbO₃ and NaTaO₃ perovskite photocatalysts. *Photochem Photobiol Sci.* 2017;16(1):17–23.
24. Ahmad T, Farooq U, Phul R. Fabrication and photocatalytic applications of perovskite materials with special emphasis on alkali metal based niobates and tantalates. *Ind Eng Chem Res.* 2018;57(1):18–41.
25. Shi H, Li X, Wang D, Yuan Y, Zou Z, Ye J. NaNbO₃ nanostructures: facile synthesis, characterization, and their photocatalytic properties. *Catal Lett.* 2009;132:205–12.
26. Paula AJ, Zaghete MA, Longo E, Varela JA. Microwave-assisted hydrothermal synthesis of structurally and morphologically controlled sodium niobates by using niobic acid as a precursor. *Eur J Inorg Chem.* 2008;2008(8):1300–8.
27. Ke T-Y, Chen H-A, Sheu H-S, Yeh J-W, Lin H-N, Lee C-Y. Sodium niobate nanowire and its piezoelectricity. *J Phys Chem C.* 2008;112(24):8827–31.
28. Yu A, Qian J, Liu L, Pan H, Zhou X. Surface sprouting growth of Na₂Nb₂O₆-H₂O nanowires and fabrication of NaNbO₃ nanostructures with controlled morphologies. *Appl Surf Sci.* 2012;258(8):3490–6.
29. Teixeira GF, Zaghete MA, Varela JA, Longo E. Synthesis and characterization of NaNbO₃ mesostructure by a microwave-assisted hydrothermal method. *Mater Res Soc.* 2014;1675:145–50.
30. Lops C, Ancona A, Di Cesare K, Dumontel B, Garino N, Canavese G, et al. Sonophotocatalytic degradation mechanisms of Rhodamine B dye via radicals generation by micro- and nano-particles of ZnO. *Appl Catal B: Environ.* 2019;243:629–40.
31. Fernandes D, Raubach CW, Jardim PLG, Moreira ML, Cava SS. Synthesis of NaNbO₃ nanowires and their photocatalytic activity. *Ceram Int.* 2021;47(7):10185–8.
32. Dovesi R, Erba A, Orlando R, Zicovich-Wilson CM, Civalleri B, Maschio L, et al. Quantum-mechanical condensed matter simulation with CRYSTAL. *WIREs Comput Mol Sci.* 2018;8(4):e1360.
33. Krukau AV, Vydrov OA, Izmaylov AF, Scuseria GE. Influence of the exchange screening parameter on the performance of screened hybrid functionals. *J Chem Phys.* 2006;125:224106.
34. Oliveira DV, Laun J, Peintinger MF, Bredow T. BSSE-correction scheme for consistent gaussian basis sets of double- and triple-zeta valence with polarization quality for solid-state calculations. *J Comput Chem.* 2019;40(27):2364–76.
35. Laun J, Oliveira DV, Bredow T. Consistent Gaussian basis sets of double- and triple-zeta valence with polarization quality of the fifth period for solid-state calculations. *J Comput Chem.* 2018;39(19):1285–90.
36. Larson AC, Von Dreele RB. GSAS. Report No. LAUR 86-748. *J Appl Crystallogr.* 1994;34:210–213.
37. Thompson P, Cox DE, Hastings, JB. Rietveld refinement of debye-scherrer synchrotron X-ray data from Al₂O₃. *J Appl Crystallogr.* 1987;20:79–83.
38. Xu H, Nyman M, Nenoff TM, Navrotsky A. Prototype sandia octahedral molecular sieve (SOMS) Na₂Nb₂O₆.H₂O: synthesis, structure and thermodynamic stability. *Chem Mater.* 2004;16(10):2034–40.
39. Jung JH, Chen C-Y, Wu WW, Hong J-II, Yun BK, Zhou Y, et al. In Situ Observation of Dehydration-Induced Phase Transformation from Na₂Nb₂O₆-H₂O to NaNbO₃. *J Phys Chem C.* 2012;116(42):22261–5.
40. Ji S, Liu H, Sang Y, Liu W, Yu G, Leng Y. Synthesis, structure, and piezoelectric properties of ferroelectric and antiferroelectric NaNbO₃ nanostructures. *Cryst Eng Comm.* 2014;16(32):7598–604.
41. Zhang D, Cheng J, Shi F, Cheng Z, Yang X, Cao M. Low temperature synthesis of ribbon-like orthorhombic NaNbO₃ fibers and their photocatalytic activities for H₂ evolution. *RSC Adv.* 2015;5(42):33001–7.
42. Teixeira GF, Ciola RA, Sakamoto WK, Zaghete MA. Perovskite-based mesostructures and related composites-influence exerted by morphology and interface. In: Barranco AP, editor. *Ferroelectric Materials-Synthesis and Characterization.* Cuba: IntechOpen, 2015;59–83.
43. Alexandre M, Bessaguet C, David C, Dantras E, Lacabanne C. Piezoelectric properties of polymer/lead-free ceramic composites. *Phase Transitions.* 2016;89(7-8):708–16.
44. Wang Y. Growth behavior and controllable morphologies of NaNbO₃ superfine particles synthesized by hydrothermal method. *Ceram Int.* 2018;44(6):7276–9.
45. Wang S, Wu Z, Chen J, Ma J, Ying J, Cui S, et al. Leadfree sodium niobate nanowires with strong piezo-catalysis for dye wastewater degradation. *Ceram Int.* 2019;45(9):11703–8.

46. Pei L, Wang J, Fan C, Ge H, Waclawik ER, Tan H, et al. The key role of photoisomerisation for the highly selective photocatalytic hydrogenation of azobenzene to hydrazobenzene over NaNbO₃ fibre photocatalyst. *J Photochem Photobiol A*. 2020;400:112655.
47. Gu Q, Zhu K, Liu J, Liu P, Cao Y, Qiu Y. Rod-like NaNbO₃: mechanisms for stable solvothermal synthesis, temperature-mediated phase transitions and morphological Evolution. *RSC Adv*. 2014;4(29):15104–10.
48. López-Juárez R, Castañeda-Guzmán R, Villafuerte-Castrejón ME. Fast synthesis of NaNbO₃ and K_{0.5}Na_{0.5}NbO₃ by microwave hydrothermal method. *Ceram Int*. 2014;40(9):14757–64.
49. Jiang X, Wang Y, Herricksb T, Xia Y. Ethylene glycol-mediated synthesis of metal oxide nanowires. *J Mater Chem*. 2004;14(4):695–703.
50. Xu Y-Q, Wu S-Y, Wu L-N, Ding C-C, Zhang L-J. Structural, elastic, electronic and optical properties of Cubic NaNbO₃ crystals under pressure. *Int J Mod Phys B*. 2018;32(25):1850282.
51. Fritsch D. Electronic and Optical Properties of Sodium Niobate: A Density Functional Theory Study. *Adv Mater Sci Eng*. 2018;2018:ID6416057.
52. Xu Y-Q, Wu S-Y, Wu L-N, Zhang L-J, Zhong S-Y. First-principles investigations on the visible light photocatalytic activity of NaNbO₃ by N and F doping. *Eur Phys J B*. 2019;92:68.
53. Wood DL, Tauc J. Weak Absorption Tails in Amorphous Semiconductors, *Phys Ver B*. 1972;5:3144–51.
54. Pan H, Wang B, Zhang F, Zhang W, Li G. Preparation and physical and photocatalytic activity of a new niobate oxide material containing NbO₄ tetrahedra. *Int J Photoenergy*. 2018;2018. <https://doi.org/10.1155/2018/8516356>
55. Raubach CW, Gouveia AF, Santana YVB, Varela JA, Ferrer MM, Li MS. Towards controlled synthesis and better understanding of blue shift of the CaS crystals. *J Mater Chem C*. 2014;2(15):2743–50.
56. Ücker CL, Gularte LT, Fernandes CD, Goetzke V, Moreira EC, Raubach CW, et al. Investigation of the properties of niobium pentoxide for use in dye-sensitized solar cells. *J Am Ceram Soc*. 2019;102(4):1884–92.
57. Teixeira GF, Junior ES, Simoes AZ, Longo E, Zaghete MA. Unveiling the correlation between structural order-disorder character and photoluminescence emissions of NaNbO₃. *Cryst Eng Comm*. 2017;19(30):4378–92.
58. Ücker CL, Riemke FC, Andrade Neto NF, Santiago A, Siebeneichler TJ, Carreño NLV et al. Influence of Nb₂O₅ crystal structure on photocatalytic efficiency. *Chem Phys Lett*. 2021;764:138271.
59. Morais LA, Adán C, Araujo AS, Guedes A, Marugán J. Synthesis, Characterization, and Photonic Efficiency of Novel Photocatalytic Niobium Oxide Materials, *Global Challenges*. 2017;1(9):1700066.

SUPPORTING INFORMATION

Additional supporting information can be found online in the Supporting Information section at the end of this article.

How to cite this article: Fernandes D, Ferrer MM, Raubach CW, Moreira ML, Jardim PLG, Moreira EC, et al. Fast synthesis of NaNbO₃ nanoparticles with high photocatalytic activity for degradation of organic dyes. *J Am Ceram Soc*. 2023;106:399–409. <https://doi.org/10.1111/jace.18740>